Disentangling superconductor and dielectric microwave losses in sub-micron Nb/TEOS-SiO_2 interconnects using a multi-mode microstrip resonator

Cougar A. T. Garcia,[1,2] Nancyjane Bailey,[1] Chris Kirby,[1] Joshua A. Strong,[1] Anna Yu. Herr,[1,3] Steven M. Anlage,[2,4] and Vladimir V. Talanov[1]

[1)] *Northrop Grumman Corp., Baltimore, MD 21240*

[2)] *Department of Materials Science and Engineering, University of Maryland, 3121 A. James Clark Hall, College Park, MD 20742, United States*

[3)] *Present address: IMEC, Leuven, Belgium*

[4)] *Quantum Materials Center, Physics Department, University of Maryland, College Park, MD 20742, United States*

(Dated: 21 March 2023)

Understanding the origins of power loss in superconducting interconnects is essential for the energy efficiency and scalability of superconducting digital logic. At microwave frequencies, power dissipates in both the dielectrics and superconducting wires, and these losses can be of comparable magnitude. A novel method to accurately disentangle such losses by exploiting their frequency dependence using a multi-mode transmission line resonator, supported by a geometric factor concept and a 3D superconductor finite element method (FEM) modeling, is described. Using the method we optimized a planarized fabrication process of reciprocal quantum logic (RQL) for the interconnect loss at 4.2 K and GHz frequencies. The interconnects are composed of niobium (Nb) insulated by silicon dioxide made with a tetraethyl orthosilicate precursor (TEOS-SiO_2). Two process generations use damascene fabrication, and the third one uses Cloisonné fabrication. For all three, TEOS-SiO_2 exhibits a dielectric loss tangent $\tan\delta = 0.0012 \pm 0.0001$, independent of Nb wire width over $0.25 - 4\ \mu m$. The Nb loss varies with both the processing and the wire width. For damascene fabrication, scanning transmission electron microscopy (STEM) and energy dispersive X-ray spectroscopy (EDS) reveal that Nb oxide and Nb grain growth orientation increase the loss above the Bardeen–Cooper–Schrieffer (BCS) minimum theoretical resistance R_{BCS}. For Cloisonné fabrication, the $0.25\ \mu m$ wide Nb wires exhibit an intrinsic resistance $R_s = 13 \pm 1.4\ \mu\Omega$ at 10 GHz, which is below $R_{BCS} \approx 17\ \mu\Omega$. That is arguably the lowest resistive loss reported for Nb.

I. INTRODUCTION

Superconducting single flux quantum (SFQ) logic relies on Josephson junctions to form the logic gates, and superconducting transmission lines to deliver clock and power to the gates as well as to propagate bits of information between various circuits on the chip.[1–6] The bits are encoded into pulses of picosecond duration and millivolt amplitude, which are generated by the junctions[7] and each carry a magnetic flux quantum $\Phi_0 \approx 2.067 \times 10^{-15}\ Wb$. With the pulse energy of $I_c\Phi_0 \sim 10^{-19}\ J$, where $I_c \sim 100\ \mu A$ is the junction critical current, and the available clock speed up to 120 GHz,[8] to compete with CMOS-based computing technologies, the SFQ logic community has been focused on the energy efficiency and scalability.[9]

Energy efficient SFQ logic families include quantum flux parametron (QFP),[3] reciprocal quantum logic (RQL),[4] energy efficient single flux quantum (eSFQ) logic,[5] and adiabatic quantum flux parametron (AQFP).[6] Analogous to Cu/low-k interconnects dominating the net CMOS power budget,[10] superconducting interconnects can notably impact the energy efficiency of SFQ logic. For instance, AC-powered RQL has been reported to be 300 times more energy efficient than CMOS, including the cooling overhead in large-scale systems.[4] However, a metamaterial zeroth order resonator (ZOR) delivering clock and power to RQL

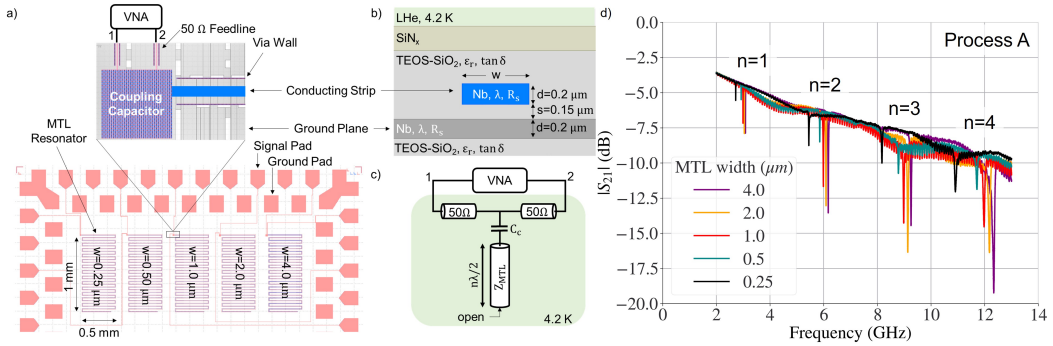

FIG. 1. a) Physical layout of a chip with five MTL resonators of conducting strip width w varying from 0.25 to 4 μm, fabricated by 3-metal-layer process. Meandering MTL takes up an area $0.5 \times 1\, mm^2$ per resonator. The zoom-in shows a "plaid" capacitor, coupling MTL resonator to 50 Ω feedline, conceptually connected to vector network analyzer VNA. On the chip, a feedline runs between two sets of ground-signal-ground contact pads. b) Diagram of the MTL cross-section, showing the nominal thicknesses. Ground plane and conducting strip are embedded into TEOS-SiO_2, and passivated with SiN_x layer. c) Conceptual diagram of the microwave test setup. The resonator is reactively coupled to the 50 Ω driving network via a coupling capacitor C_c. VNA applies RF power, and measures the transmission coefficient S_{21} at 4.2 K. d) Representative $|S_{21}|$ spectra for five MTL resonators from one of the chips fabricated by *Process A*. Resonant dips marked by the mode index $n = 1 - 4$ correspond to the first four TM_{00n} modes. The sloped background is due to the signal attenuation in a cryogenic dip probe.

gates at GHz frequencies dissipated twice more power than the logic junctions, due to the loss in transmission lines forming the ZOR.[11]

Interconnect density remains one of the main factors limiting the scalability of all forms of superconducting logic.[12] The performance capability of an SFQ logic chip increases with the total number of logic gates, which calls for more interconnect layers with smaller wire width and spacing (pitch). Reducing the wire cross-section to deep sub-micron dimensions, where it becomes comparable to or smaller than the superconductor magnetic penetration depth $\lambda \sim 90\, nm$ in Nb, creates complex requirements to fabricate high-bandwidth, low-loss interconnects. Chemical mechanical polishing or planarization (CMP)[13] allows one to fabricate an SFQ logic chip with up to ten wiring layers,[14] by removing topography left from the previous layer patterning and deposition.[15–17] In our work, both the damascene (metal CMP) and Cloisonné (dielectric CMP) planarized processes will be utilized and compared. We will present an elemental material analysis to reveal possible sources of extrinsic microwave loss in the sub-micron Nb interconnects.

The microstrip transmission line (MTL) and stripline are the ubiquitous superconducting interconnects, with 700 GHz analog bandwidth. On one hand, they can provide a basic building block for GHz clock and power distribution systems.[11,18,19] On the other hand, they can form a passive transmission line, to propagate low-bandwidth (35-50 GHz) data with 7-10 SFQ pulses per bit,[19] or to propagate high-bandwidth (350 GHz) data with single SFQ pulse per bit,[20,21] or to produce a delay-line memory.[22] The power dissipation is governed by the superconductor and dielectric loss, and is inversely proportional to a transmission line resonator figure of merit, quality factor (Q-factor).[23] Similarly, the propagation distance of SFQ pulse scales with the Q-factor.[21] Our paper is concerned with simultaneously extracting the superconductor microwave resistance R_s and the insulator loss tangent $\tan\delta$ from experimental Q-factor data on MTL resonators, at an RQL operating temperature of liquid helium (LHe) $T = 4.2\, K$.

Resonant structures provide the most sensitive way to measure R_s[24–34] and $\tan\delta$[35–39] at microwave frequencies. We shall employ finite-length sections of MTL, with open-circuit boundary conditions at the ends, to act as MTL resonators, enabling sensitive measurements of loss and inductance.[40–44] A resonator Q-factor is defined as $Q = 2\pi f_r W/P \gg 1$, where

f_r is the resonant frequency, W is the energy stored in the resonator, and P is the net power lost by the resonator. In practice, one measures the loaded Q-factor

$$\frac{1}{Q_l} = \frac{1}{Q_i} + \frac{1}{Q_e} = \frac{1}{Q_c} + \frac{1}{Q_d} + \frac{1}{Q_r} + \frac{1}{Q_e} \tag{1}$$

where Q_i is the internal (unloaded) Q-factor, Q_e is the external (coupling) Q-factor associated with the resonator excitation, and Q_c, Q_d and Q_r are the partial Q-factors associated with the conductor, dielectric and radiation power loss, respectively. The coupling contribution Q_e can be removed by modern analysis techniques.[45,46] The radiation loss[47] is typically negligibly small and can be ignored. Since Q_c^{-1} and Q_d^{-1} are additive, the corresponding conductor and dielectric loss contributions are inseparable. To disentangle them, resonant techniques either postulate the "unwanted" loss, or exploit regimes where Q_i is dominated by the "wanted" loss. The $Q_c \ll Q_d$ regime favors the measurement of R_s. The $Q_d \ll Q_c$ regime favors the measurement of tanδ.

Superconducting cavity[24,25,28,29] and quasi-optical[31] resonators measure R_s of bulk and thin-film superconductors by attaining $Q_c \ll Q_d$. To deduce R_s of superconducting thin films using a dielectric resonator technique,[32] one must presume a tanδ value for the dielectric puck. Tuckerman *et al.* measured tanδ of Nb/polyimide flexible transmission line tapes in the $Q_d \ll Q_c$ regime, at 1.2 K and 20 mK where the Nb loss becomes negligible.[38] Quantum computing resonators attain $Q_d \ll Q_c$ at mK temperatures, to characterize a two-level-system dielectric loss.[39] Kaiser exploited $Q_d \ll Q_c$ in the Nb lumped element resonator, to investigate frequency dependence of tanδ for amorphous thin-film dielectrics at 4.2 K.[37] Oates *et al.* reported that at 4 K, losses in Nb/SiO_2 sub-micron stripline resonators are limited by the dielectric except for the narrowest strips, although they did not deduce tanδ or R_s.[48] Krupka *et al.* optimized a dielectric resonator for $Q_d \ll Q_c$, to measure the loss tangent of isotropic low-loss dielectrics[36] and high-resistivity silicon[49] at room temperature. Taber overcame the above limitations by varying the dielectric spacer thickness (geometric factor) of the superconducting parallel-plate resonator,[30] which allows to deduce both R_s and tanδ.[30,33] However, this approach is impractical for characterization of patterned interconnects.

In contrast to existing work, we shall extract both the superconductor and dielectric loss by exploiting their frequency dependence in a multi-mode MTL resonator. In fact, we shall take advantage of both losses in our structures being of comparable magnitude $Q_c \sim Q_d$, owing to interplay between the MTL geometry and loss. Fitting theoretical model to experimental dependence of $Q_i^{-1} = Q_c^{-1} + Q_d^{-1}$ on the resonant frequency allows us to quantitatively de-convolve the two losses in a single measurement.

Analytical or numerical modeling of superconducting interconnects[20,50–54] typically relies on the Leontovich boundary condition, commonly referred to as a surface impedance boundary condition (SIBC).[55–58] It approximates the transmitted wave as a wave propagating normal to the surface of an imperfect conductor, regardless of the incident angle. SIBC is immensely fruitful for electrically-large systems[25,26,28,32–34,59] with the conductor surface curvature radius much greater than the penetration depth λ. The SIBC approximation is inapplicable to an interconnect with the cross-section comparable to or smaller than λ.

To overcome this limitation for submicron MTLs, we shall deal the *intrinsic* impedance $Z_s = R_s + iX_s = \sqrt{i\mu_0\omega/\sigma}$, where X_s is the microwave reactance, μ_0 is the vacuum permeability, $\omega = 2\pi f$ is the angular frequency with f being the linear frequency, and $\sigma = \sigma_1 - i\sigma_2$ is the superconductor complex conductivity.[60] A finite element method (FEM) simulation can provide the field and current distributions within the wire,[21,61] which for a good superconductor of $\sigma_1 \ll \sigma_2$, or $R_s \ll X_s$, are defined by the superfluid electrons distribution, that is σ_2 or λ. This allows us to derive a relationship between Q_c and R_s via a geometric factor defined by the MTL cross-section and λ. Simulating the MTL geometric factor using Ansys' 3D electromagnetic FEM modeler,[62] we investigate R_s and tanδ as functions of Nb wire width down to 0.25 μm. FEM modeling can also address the fabrication effects impacting interconnects, such as irregular cross-section shape and rounded edges of the wire, critical dimensions miss-targeting and variation across the wafer, intermixing of materials at the interface, etc.

This paper is organized as follows. First, we will describe design, fabrication, and RF characterization of a multi-mode MTL resonator. After presenting data for the frequency dependence of internal Q-factor, we will introduce analytical theory to fit them. Next, a resonator geometric factor, involved into the theory, will be obtained from 3D FEM simulations. Finally, the superconductor and dielectric losses will be deduced, and their dependence on the MTL width and processing conditions will be discussed with the aid of a microscopic analysis.

II. RESONATOR DESIGN, FABRICATION, AND CHARACTERIZATION

A. Design and layout

To implement the proposed concept, we designed a chip containing five half-wavelength-long open-ended MTL resonators shown in Fig. 1(a), representative of RQL interconnects. The MTL is formed by a Nb ground plane and a Nb conducting strip, embedded into silicon dioxide derived from tetraethyl orthosilicate (TEOS-SiO_2), as depicted in Fig. 1(b). The conducting strip width w varies from 0.25 to 4 μm. Each resonator is folded into a meander shape to conserve space. Via walls surround the conducting strip, to facilitate RF isolation between the adjacent meander sections.

A superconducting MTL supports a slow TM_{00} wave.[63,64] A resonant condition $\beta l_{res} = \pi n$ yields the MTL resonator eigen frequencies

$$f_n = \frac{n}{2l_{res}\sqrt{LC}} \approx \frac{nc}{2l_{res}\sqrt{\varepsilon_r}}\sqrt{\frac{s}{s+2\lambda\coth(d/\lambda)}} \tag{2}$$

where $\beta = \omega\sqrt{LC}$ is the phase constant, l_{res} is the resonator geometrical length, $n = 1, 2, 3...$ is the longitudinal mode index, and L and C are the series inductance and shunt capacitance per unit length given in Appendix A, Eqs. A2b and A2d. The approximation on the right in Eq. 2 holds for a wide MTL (parallel-plate waveguide) with $w \gg s$, where s is the dielectric spacing between the strip and ground plane,[33] c is the speed of light in vacuum, ε_r is the relative dielectric constant, and d is the superconductor wire thickness. The resonator frequency was designed based upon the material nominal properties ($\varepsilon_r = 4.2$, $\lambda = 90\,nm$) and fabrication thicknesses ($s = 150\ nm$, $d = 200\ nm$) shown in Fig. 1(b). The selected resonator length $l_{res} = 15\ mm$ is a trade-off between fitting many resonators on a single $5\times5 mm^2$ chip, and accommodating many resonant modes within the test setup bandwidth. With the above parameters, Eq. 2 predicts a fundamental frequency $f_1 \approx 3.27$ GHz. That frequency, measured for a $4\mu m$ resonator, is $f_1 = 3.20\pm0.07$GHz, which is within 0.8% of the above estimate. This agreement supports our assumed values of $\varepsilon_r \approx 4.2$ for TEOS-SiO_2,[65] and $\lambda \approx 90\,nm$ for Nb. The latter was verified by SQUID inductance measurements[66] and agrees with Ref.[67]

Each resonator is reactively coupled to a microstrip feedline through a coupling capacitor, as shown in Fig. 1(a) zoom-in. Figure 1(c) conceptualizes the RF driving network for our resonators. To overcome the parasitic ripple in transmission coefficient caused by impedance discontinuities in the measurement system (see Fig. 1(d)), we realized about 6 dB insertion loss at the resonance. For a reactively coupled resonator, this corresponds to the critical coupling coefficient $g \equiv Q_i/Q_e = 1$. The network in Fig. 1(c) can be modeled as a shunt load, with the transmission coefficient $S_{21} = 2Z_{in}/(Z_0 + 2Z_{in})$,[23] where Z_{in} is the input impedance seen at the T-junction looking toward the coupling capacitor, and $Z_0 = 50\ \Omega$ is the feedline characteristic impedance. At the resonant frequency, $Z_{in} = R_{in}$ is purely real, and $S_{21} = (1+g)^{-1}$ per Ref.,[68] which lead to $2R_{in}/(Z_0 + 2R_{in}) = (1+g)^{-1}$. Inserting here the input resistance for a gap-coupled half-wavelength open-ended resonator[23] $R_{in} = (8\pi f_n^2 C_c^2 Z_{MTL} Q_i)^{-1}$, and solving the resulting equation for the coupling capacitance C_c, gives

$$C_c = \frac{1}{2f_n}\sqrt{\frac{g}{\pi Z_0 Z_{MTL} Q_i}} \tag{3}$$

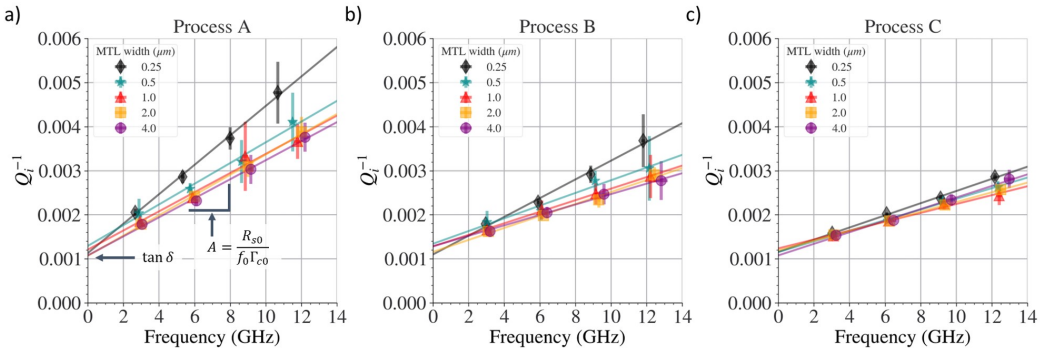

FIG. 2. The reciprocal internal Q-factor Q_i^{-1} of MTL resonator at 4.2 K versus the resonant frequencies f_n for the first four modes $n = 1 - 4$. Each graph shows results for all five MTL resonators of varying width $w = 0.25 - 4\ \mu m$, fabricated by a) *Process A*, b) *Process B*, and c) *Process C*. Q_i was extracted from S_{21} spectra like ones shown in Fig. 1(d). The solid lines are linear fits of Eq. 8 to data for each MTL width fabricated by respective process. The fit slope A is proportional to the Nb microwave resistance R_s taken at a reference frequency f_0, and the fit y-intercept yields the TEOS-SiO_2 dielectric loss tangent tanδ at GHz frequencies.

where $Z_{MTL} = \sqrt{L/C}$ is the MTL characteristic impedance. Inserting f_1 given by Eq. 2, $g = 1$, L and C given by the parallel-plate approximation Eqs. A2b, A2d in Appendix A, and Q_i of a parallel-plate resonator[33] into Eq. 3 provides the design value for a coupling capacitor. For our MTL resonators, C_c ranges from 50 to 250 fF, corresponding to MTL widths ranging from 0.25 to 4 μm.

To enable such capacitors in a damascene process, where large metal patches are disallowed because of the requirement to limit the metal coverage density, a "plaid" capacitor design was used (see Fig. 1(a), zoom-in). It is formed by multiple parallel wires running in one metal layer, and many more parallel wires running in the adjacent metal layer perpendicular to the wires in the first layer. Two interleaved square grids of vias connect every other wire in the first layer to every other wire in the second layer. This creates two interwoven electrodes with about the same capacitance per unit area as a parallel plate capacitor.

B. Fabrication

MTL resonators were fabricated by three generations of a 3-metal-layer process with 0.25 μm minimum feature size. Throughout the paper these will be referred to as *Processes A*, *B*, and *C*. In all three of them, the metal Nb is made by physical vapor deposition, and the insulator SiO_2 is made by low-temperature plasma enhanced chemical vapor deposition[69] from a tetraethoxysilane $Si(OC_2H_5)_4$ (TEOS) precursor. *Process A* is an inverted MTL geometry using a damascene process with the ground plane on the second layer. *Process B* is a non-inverted MTL geometry using a damascene process with the ground plane on the first layer. *Process C* is a non-inverted MTL geometry using a Cloisonné process with the ground plane on the first layer. Figure 1(b) depicts the cross-sectional geometry of the MTL fabricated by *Processes B* or *C*.

The damascene process begins with depositing a uniform layer of dielectric on a planarized surface. After the trenches or vias corresponding to interconnects are defined by photolithography and subtractively patterned using reactive-ion etching (RIE), metal is deposited to fill and overfill (overburden) the trenches or vias. Finally, CMP polishes away the excess metal until the intermetal dielectric, embedding the wires or vias, is exposed. To promote adhesion of TEOS-SiO_2 to Nb, the planarized surface is treated with an oxygen plasma. The smooth surface is now ready for the next layer.

The Cloisonné process begins with depositing a uniform layer of interconnect metal on a planarized surface. After the interconnects are defined by photolithography and subtractively patterned using RIE, the dielectric is deposited conformally over the metal features. Once metal is completely embedded with dielectric, the resulting surface is planarized by CMP to remove the excess dielectric, until the wires or vias are exposed. The surface is now ready for the next layer.

C. Experimental

From each process, 6 to 9 chips selected within the inner 80 mm diameter of the 150 mm wafer were tested. Measurements were taken at $4.2K$ in a LHe Dewar using an RF dip probe equipped with a 32-contact-pad test fixture.[11,18,19,21] To provide for fast sample exchange, a flip-chip press-contact technology is used, where the chip contact pads are pressed against the fixture non-magnetic Cu/Au bumps. The fixture PCB interfaces the bumps to the probe semi-rigid coaxial cables. During experiment, the fixture and roughly 30 cm of the dip probe were immersed in a LHe bath. The S-parameters were measured by a Keysight N5222A 2-port vector network analyzer (VNA), with the test cables calibrated to the top of the probe. To minimize the possibility of non-linear effects[70–72] in MTL resonators, the microwave power entering the chip was kept below 10 μW.

Figure 1(d) shows representative transmission coefficient magnitude $|S_{21}|$ vs. frequency for one of the chips made by *Process A*. The probe bandwidth of 14 GHz limited the measurements to the first four modes $n = 1 - 4$ of the MTL resonators. To extract the internal Q-factor Q_i and the resonant frequency f_n from the complex S_{21} data, we subtract a phase delay due to the probe cables and employ a diameter correction method.[45,46,73] Depending on the fabrication process, MTL geometry, and mode index, we observed Q_i between 200 and 700.

Figure 2 shows Q_i^{-1} obtained from 4 wafers on a total of 22 chips (5 MTL resonators per chip). Each panel of Fig. 2 shows Q_i^{-1} as a function of resonant frequency for all five MTL widths, for particular fabrication process. Each data point and error bar represent the arithmetic mean and 1 standard deviation for a sample of 6-9 chips per process, to statistically describe the loss variation for each respective MTL width for each process. The increased error bars for modes $n = 3, 4$ in *Processes A* and *B* are due to parasitic ripple in $|S_{21}|$ seen in Fig. 1(d). Evaluating a measurement repeatability by re-inserting the same chip several times into a test fixture, yielded maximum spread in the extracted Q_i and f_n of $<10\%$ and $<0.1\%$, respectively.

III. DATA ANALYSIS

To explain the nearly linear dependence of Q_i^{-1} on resonant frequency observed in Fig. 2, a geometric factor concept devised in Appendix A allows to express Q_i as

$$\frac{1}{Q_i} = \frac{1}{Q_c} + \frac{1}{Q_d} = \frac{R_s^{gp}}{\Gamma_c^{gp}} + \frac{R_s^{cs}}{\Gamma_c^{cs}} + \frac{\tan\delta}{\Gamma_d} \tag{4}$$

where R_s^{gp} and R_s^{cs} are the intrinsic resistances of the ground plane and conducting strip, Γ_c^{gp} and Γ_c^{cs} are the partial geometric factors associated with resistive loss in the ground plane and conducting strip, $\tan\delta$ is the TEOS-SiO_2 dielectric loss tangent, and Γ_d is the geometric factor associated with loss in the TEOS-SiO_2. By making assumptions about the frequency dependence of R_s and $\tan\delta$, we shall factor out the frequency in Eq. 4.

A frequency dependence for R_s can be written as

$$R_s = R_{s0}(\omega/\omega_0)^\alpha \tag{5}$$

where $R_{s0} = R_s(\omega_0)$ is the intrinsic resistance at a reference frequency $\omega_0 = 2\pi f_0$ that we choose $f_0 = 10$ GHz. Although a BCS theory predicts that the scaling exponent α

decreases from 1.8 to 1.7 over 1–10 GHz for Nb at 4.2 K, the experiments show that the smearing density of states makes $\alpha \approx 2$ up to 10 GHz,[26,74] which roughly corresponds to the frequency span of our resonators. For an isotropic good superconductor with $\sigma_1 \ll \sigma_2$, the two-fluid model also predicts $\alpha = 2$.[26,27]

A dielectric loss tangent can be expressed as $\tan\delta = \sigma_d/\varepsilon_0\varepsilon_r\omega$, where σ_d is the material conductivity, and ε_0 is the vacuum permittivity.[23] According to Jonscher's universal relaxation law, σ_d scales with frequency as $\sigma_d = \sigma_{DC} + P\omega^p$, where σ_{DC} is the DC conductivity, P is the exponential prefactor, and the exponent p falls in the range of $0 < p \leq 1$.[75] Then, at frequencies high enough that $\sigma_{DC} \ll P\omega^p$, a frequency dependence for $\tan\delta$ can be written as

$$\tan\delta = \tan\delta_0(\omega/\omega_0)^{p-1} \tag{6}$$

where $\tan\delta_0 = P\omega_0^{p-1}/\varepsilon_0\varepsilon_r$ is the loss tangent at a reference frequency ω_0. Jonscher proposed that low-loss dielectrics with $\tan\delta < 0.1$ have a nearly "flat loss", that is $p \to 1$, over several decades of frequency.[75] However, $\tan\delta$ can also increase approximately linearly with frequency in some ceramics, glasses and polymers,[35,76] corresponding to $p \approx 2$ in Eq. 6.

Recalling that $\Gamma_c \propto \omega$ per Eq. A5a, application of Eqs. 5 and 6 to Eq. 4 gives

$$\frac{1}{Q_i} = \left(\frac{R_{s0}^{gp}}{\Gamma_{c0}^{gp}} + \frac{R_{s0}^{cs}}{\Gamma_{c0}^{cs}}\right)\left(\frac{\omega}{\omega_0}\right)^{\alpha-1} + \frac{\tan\delta_0}{\Gamma_d}\left(\frac{\omega}{\omega_0}\right)^{p-1} \tag{7}$$

where the quantities with subscript "0" are taken at a reference frequency ω_0. Considering $\alpha = 2$ for Nb, the linear dependence of Q_i^{-1} with frequency in Fig. 2 suggests $p \approx 1$ in Eq. 7. This implies that for all three processes TEOS-SiO_2 has a "flat loss" over at least 3-13 GHz. That result agrees with Tuckerman *et al.*,[38] who observed similar behavior in a Nb/polyimide transmission line resonator at 4.2 K over 2-20 GHz. However, Kaiser[37] reported $0.57 \leq p \leq 0.68$ for various amorphous thin-film dielectrics at 4.2 K and 0.1-20 GHz, although he ignored the Nb loss in a lumped element resonator.

An embedded MTL like in Fig. 1(b) has $\Gamma_d \approx 1$. Then, setting $\alpha = 2$ and $p = 1$ in Eq. 7 leads to the linear form

$$Q_i^{-1} = \frac{R_{s0}}{f_0\Gamma_{c0}}f + \tan\delta = Af + \tan\delta \tag{8}$$

where $R_{s0} = (R_{s0}^{gp}\Gamma_{c0}^{cs} + R_{s0}^{cs}\Gamma_{c0}^{gp})/(\Gamma_{c0}^{gp} + \Gamma_{c0}^{cs})$ represents the MTL net resistive loss, and $\Gamma_{c0} = (1/\Gamma_{c0}^{gp} + 1/\Gamma_{c0}^{cs})^{-1}$ is the net conductor geometric factor. $R_{s0} = R_{s0}^{cs} = R_{s0}^{gp}$ in the case of the homogeneous MTL. Fitting Eq. 8 to the data sets in Fig. 2 with $A = R_{s0}/f_0\Gamma_{c0}$ and $\tan\delta$ being the fitting parameters, the fit slope A is proportional to R_{s0}, and the fit y-intercept is $\tan\delta$.

Figure 2 shows that *Process A* exhibits larger fit slope A, hence higher superconductor loss, for all MTL widths relative to *Processes B* and *C*. For MTL width 1 μm and under, *Process B* has higher superconductor loss in comparison to *Process C*, while for the 2- and 4-μm-wide MTLs *Processes B* and *C* yield similar loss. Furthermore, all MTL widths and processes yield roughly the same y-intercept, corresponding to $\tan\delta \approx 0.0012$.

Equation 8 infers that the MTL superconductor loss can be deduced from the fit slope A as

$$R_{s0} = Af_0\Gamma_{c0} \tag{9}$$

For the wide MTL with $w \gg s$, the conductor geometric factor can be found from a parallel-plate model[33]

$$\Gamma_{c0}^{PP} = \omega_0\mu_0\frac{s + 2\lambda\coth(d/\lambda)}{2[\coth(d/\lambda) + (d/\lambda)\,\mathrm{csch}^2(d/\lambda)]} \tag{10}$$

Finding Γ_c for the narrow MTL with $w \lesssim s$ calls for FEM modeling because the parallel-plate approximation accounts for neither the current concentration at the edges of conducting strip[61] nor the field fringing[77] nor the case of irregular geometry of the conducting strip.[78]

Equation 1 infers that a resonator optimized for simultaneous characterization of both superconductor and dielectric losses calls for $Q_c = Q_d$, which according to Eq. 8 corresponds to a conductor geometric factor $\Gamma^*_{c0} = R_{s0}/\tan\delta$. For representative $R_{s0} = 20\ \mu\Omega$ and $\tan\delta = 10^{-3}$, one estimates $\Gamma^*_{c0} = 20\ m\Omega$. For the MTL geometry depicted in Fig. 1(b), Eq. 10 predicts $\Gamma^{PP}_{c0} \sim 12\ m\Omega$ at 10 GHz and 4.2 K, which is close to Γ^*_{c0}. This makes our MTL resonators sensitive to both types of loss.

IV. FEM MODELING

In our work, the conductor geometric factor Γ_c depends on the field and current distributions inside the wires (see Eqn. A5a). Arguably, Ref.[61] is the only paper solving these for a superconducting strip transmission line, using a proprietary FEM solver. We employ Ansys' High Frequency Structure Simulator (HFSS)[62] to find geometric factors of the MTL resonators.

HFSS is a full 3D FEM simulator, capable of solving fields, currents, and network parameters for virtually any microwave structure with the ratio of largest to smallest dimension less than 10^4. The peculiar aspects of modeling a superconductor network in HFSS are (i) defining the lossy superconductor material by a real conductivity and a negative permittivity;[79] (ii) using perfect electric conductor (PEC) material to connect superconductor members to the ports, since HFSS does not allow superconducting ports;[80] (iii) enforcing the *solve-inside* option for the superconductor material, to override the HFSS default setting of only solving inside a material when the conductivity is less than $10^5\ S/m$.

A. Defining a superconductor in HFSS

Inserting the superconductor current-field constitutive relationship $\mathbf{J} = (\sigma_1 - i\sigma_2)\mathbf{E}$ into Maxwell's curl-H equation yields

$$\nabla \times \mathbf{H} = \sigma_1 \mathbf{E} + i\omega\varepsilon_0 \left(\varepsilon - \frac{\sigma_2}{\varepsilon_0 \omega}\right) \mathbf{E}$$

where the parenthesis enclose the superconductor relative permittivity $\varepsilon_{sc} = \varepsilon - \frac{\sigma_2}{\varepsilon_0\omega}$, with ε being the ordinary dielectric constant associated with displacement current. Modeling a superconductor as a collisionless neutral plasma[79,81] with Langmuir frequency $\omega_p = c/\lambda$ and dielectric function $\varepsilon_p = 1 - (\frac{\omega_p}{\omega})^2 = 1 - (\frac{c}{\omega\lambda})^2$, comparison of ε_{sc} and ε_p infers that $\varepsilon = 1$ is the superconductor permittivity in the limit $\omega \gg \omega_p$,[82] and $\sigma_2 = 1/\omega\mu_0\lambda^2$ is the London conductivity. Therefore, a lossy superconductor can be defined as a material with real conductivity $\sigma_{sc} = \sigma_1$ and real permittivity $\varepsilon_{sc} = 1 - \frac{\sigma_2}{\varepsilon_0\omega}$, applicable over the entire range of temperatures and frequencies of interest. Owing to $\sigma_2 \gg \varepsilon_0\omega$, a superconductor permittivity is substantially negative quantity.[83]

Generally, the Mattis-Bardin theory allows to tabulate σ_{sc} and ε_{sc} as HFSS *datasets*.[21] Here, exploiting the assumption $\sigma_1 \ll \sigma_2$, we define a superconductor in HFSS as a frequency-dependent material. Relating σ_1 to the experimental intrinsic resistance and penetration depth, a two-fluid model gives $\sigma^{HFSS}_{sc} = 2R_{s0}/\omega_0^2\mu_0^2\lambda^3$ that is frequency independent. By the same assumption, modeling σ_2 as the London conductivity gives $\varepsilon^{HFSS}_{sc} = -(c/\omega\lambda)^2$. Adapting HFSS to solve *inside* the superconductor overcomes a limitation of SIBC-based models[50–54] to an interconnect with a much bigger cross-section than λ.

B. Modeling a superconducting MTL in HFSS

Figure 3(a) shows 3D HFSS model of a two-port network formed by a superconductor MTL with PEC ports of the same cross-sectional geometry.[21] Note that to determine Γ_c, we simply model a piece of uniform MTL, not an MTL resonator. To achieve accurate results,

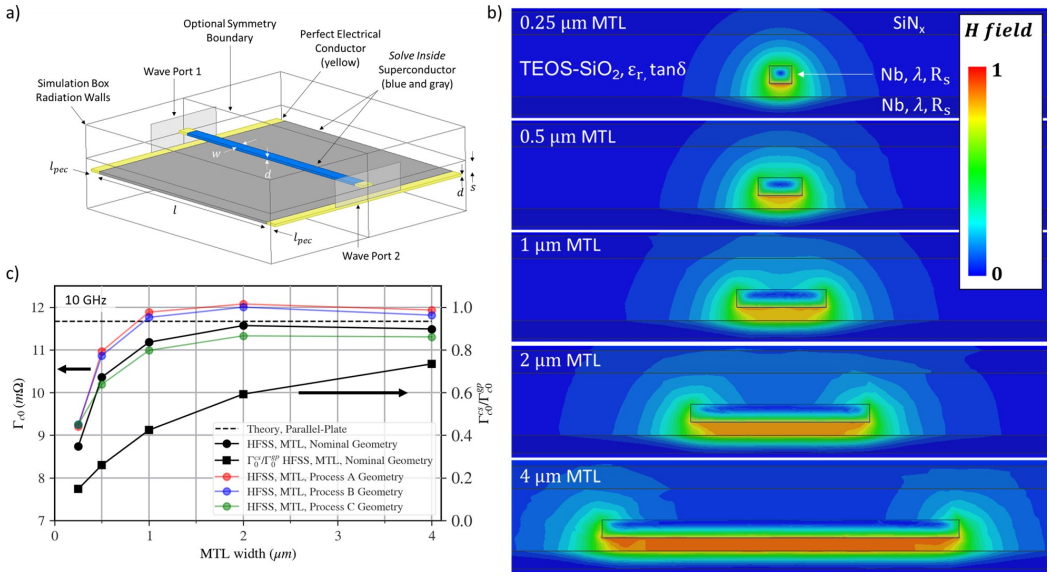

FIG. 3. a) The HFSS model of a superconducting MTL. A conducting strip (blue) of width w is separated by a dielectric spacing (transparent) of thickness s from a ground plane (gray). Both the strip and ground plane have same thickness d and simulation length l. The MTL is enclosed by a simulation box with all faces set as *Radiation* boundaries. To stimulate the model, PEC members (yellow) connect the wave ports to the superconductor ground plane and conducting strip. b) Magnetic field intensity looking into MTL cross-section, simulated at 10 GHz. The MTL width varies from 0.25 to 4 μm, top to bottom. Here, $s = 150\,nm$, $d = 200\,nm$, the Nb magnetic penetration depth and intrinsic resistance are $\lambda = 90\,nm$ and $R_s = 20\,\mu\Omega$, the TEOS-SiO_2 relative dielectric constant and loss tangent are 4.2 and 10^{-3}, and the SiN_x relative dielectric constant and loss tangent are 7.5 and 10^{-4}. c) The net conductor geometric factor Γ_c taken at 10 GHz versus MTL width, found from HFSS solver using Eq. 12 for the nominal cross-sectional geometry (black circles), and for the fabricated geometries for all three processes (red, green, and blue circles). Dashed black line is a parallel-plate approximation using Eq. 10. The black squares show the geometric factor ratio $\Gamma_{c0}^{cs}/\Gamma_{c0}^{gp}$. Solid lines are a guide to the eye.

the model is electrically short $\beta l \ll 1$, with l being the length of the MTL piece, and the PEC port length is a small fraction of the simulated transmission line $l_{pec} \ll l$. The *network analysis driven terminal* solution type[62] was used to simulate MTL lengths $l = 10 - 50\,\mu m$ with PEC port length $l_{pec} = 1\,\mu m$, at simulation frequency 10 GHz. PEC ports were de-embedded to get only the network parameters pertaining to the superconductor MTL.

All geometries and material definitions were parameterized and the *Optimetrics* option was used for parameter sweeps. To provide for fast and accurate simulation, the HFSS convergence criteria was set at 0.1-1% for the *RLGC* parameters defined as $R^{HFSS} = \mathrm{Re}(Z)$, $L^{HFSS} = \mathrm{Im}(Z)/\omega$, $G^{HFSS} = \mathrm{Re}(Y)$, and $C^{HFSS} = \mathrm{Im}(Y)/\omega$.[84] Here, Z and Y are the series impedance and shunt admittance of a general transmission line,[85] given by

$$Z = 2(Z_{11} - Z_{12})l^{-1} \tag{11a}$$

$$Y = Z_{12}^{-1} l^{-1} \tag{11b}$$

where Z_{11} and Z_{12} are the elements of the network [Z]-matrix found by HFSS, as described in Appendix B. It is tractable to complete parametric sweeps on the order of 100 simulations in a few hours.

Figure 3(b) shows the magnetic field intensity looking into MTL cross-section, for all five MTL widths, in the case of the nominal geometry and material parameters for *Processes B* and *C*. For 2 μm wide MTL and above, the magnetic field distribution has a parallel-plate-like geometry. For 1 μm MTL and below, the magnetic field penetrates the majority of the

conducting strip, but only a small fraction of the ground plane.

C. Deducing geometric factor from HFSS

Setting the dielectric loss in the HFSS model to zero leads to $Q_i = Q_c$. The net conductor geometric factor can be found from HFSS simulations, ran at a reference frequency ω_0, as

$$\Gamma_{c0} = R_{s0}^{HFSS} \frac{\omega_0 L^{HFSS}}{R^{HFSS}} \tag{12}$$

where R_{s0}^{HFSS} is the intrinsic microwave resistance corresponding to σ_{sc}^{HFSS}. Likewise, the partial geometric factor of just the conducting strip can be found by setting the ground plane loss to zero in the above procedure, and vice versa for the ground plane geometric factor. For each MTL geometry, only a single simulation for any resistance value meeting $R_{s0}^{HFSS} \ll \omega_0 \mu_0 \lambda$ is required, which substantially accelerates the data analysis. We hypothesize that geometric factor can also be computed by numerically integrating Eq. A5a with the fields and currents found by an FEM simulator (see Fig. 3(b)).

The geometric factors found using HFSS were verified to be independent of R_{s0}^{HFSS} between 0.1 and 100 $\mu\Omega$. The HFSS results were further validated by comparing the geometric factor by Eq. 12 to the parallel-plate approximation Eq. 10. Figure 3(c) shows that Γ_c for the MTL with nominal geometry (black solid line) approaches Γ_c^{PP} (black dashed line) within 1.5% at 2 μm MTL width and above. Intuitively, this can be understood from Figure 3(b), where the fringing fields above the conducting strip begin to overlap below a 2 μm width. Hence, Eq. 10 can be used for preliminary data analysis in wide MTLs with $w/s > 13$, without resorting to HFSS simulations.

V. RESULTS AND DISCUSSION

The cross-sectional geometries for each *Process* and MTL width were measured by focused ion beam (FIB) or scanning transmission electron microscopy (STEM). These actual geometries, including slanted sidewalls of conducting strip, were modeled in HFSS to find the conductor geometric factor Γ_{c0} using Eq. 12. Finally, such actual geometric factors shown in Fig. 3(c) were utilized to deduce the MTL net intrinsic resistance R_{s0} from the linear fits in Fig. 2 using Eq. 9.

Figure 4 shows the results vs MTL width. The error bars in Fig. 4(a) are obtained by applying the error propagation analysis to Eq. 9, neglecting correlations. The uncertainties in the fit slope A and the y-intercept $\tan\delta$ are estimated from the linear regression in Fig. 2. The uncertainty in Γ_c is found using HFSS to model the effects of MTL geometry variations across the wafer.[84]

Since the ratio $\Gamma_{c0}^{cs}/\Gamma_{c0}^{gp} \leq 1$ decreases with MTL width per Fig. 3(c), the smaller the width, the greater the conducting strip contribution into R_{s0}. In the case of dissimilar $R_s^{cs} \neq R_s^{gp}$, the R_{s0} in Eq. 8 can be written as

$$\begin{aligned} R_{s0} &= R_{s0}^{cs} \frac{1 + (\Gamma_{c0}^{cs}/\Gamma_{c0}^{gp})(R_{s0}^{gp}/R_{s0}^{cs})}{1 + \Gamma_{c0}^{cs}/\Gamma_{c0}^{gp}} \\ &\approx R_{s0}^{cs} \left[1 - \frac{\Gamma_{c0}^{cs}}{\Gamma_{c0}^{gp}} \left(1 - \frac{R_{s0}^{gp}}{R_{s0}^{cs}} \right) \right] \end{aligned} \tag{13}$$

where the approximation holds for $\Gamma_{c0}^{cs}/\Gamma_{c0}^{gp} \ll 1$. For the 0.25 μm wide MTL, assuming $R_{s0}^{gp} \sim R_{s0}^{cs}$, the ratio $\Gamma_{c0}^{cs}/\Gamma_{c0}^{gp} \sim 0.14$ means that the corresponding R_{s0} in Fig. 4(a) is dominated by the strip loss.

Figure 4(a) reveals that for all MTL widths, the Nb loss reduces from *Process A* to *Process B* to *Process C*. Our medium-loss *Process B* has R_{s0} in the $14 - 20$ $\mu\Omega$ range. This is in agreement with $R_{s0} \approx 16$ $\mu\Omega$ measured by the parallel-plate resonator for Nb thin films at

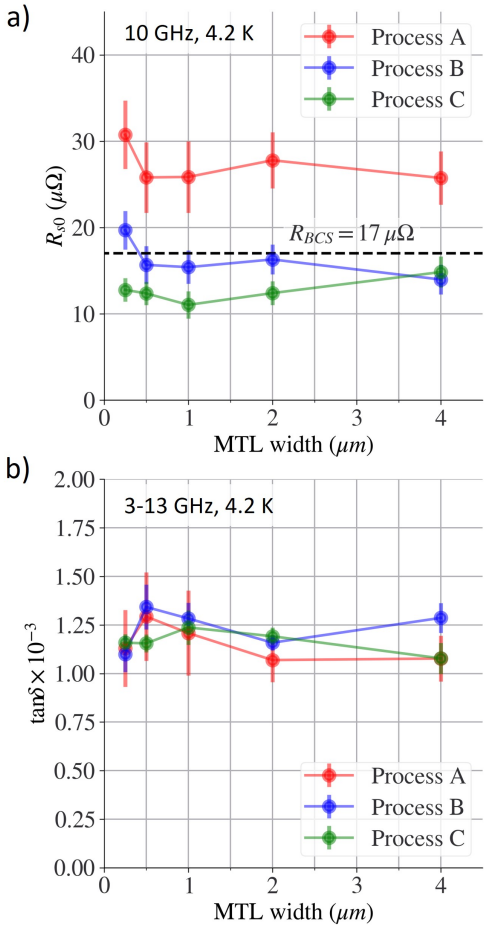

FIG. 4. (a) The MTL net intrinsic resistance at 10 GHz, 4.2 K versus MTL width and fabrication process, deduced from the fit slope A in Fig. 2 using Eq. 9 and the geometric factor Γ_{c0} given by Eq. 12. The black dashed line represents the BCS theoretical minimum for Nb.[28,86] (b) TEOS-SiO_2 loss tangent tanδ at 4.2 K versus MTL width and fabrication process given by the fit y-intercept in Fig. 2. Solid lines are a guide to the eye.

4.2K, 12 GHz[30] and scaled to 10 GHz using Eq. 5. Our result is also in agreement with the Bardeen–Cooper–Schrieffer (BCS) minimum intrinsic resistance $R_{BCS} \approx 17\ \mu\Omega$ measured by Benvenuti *et al.* using the RF cavity with thin-film Nb walls at 4.2 K, 1.5 GHz[28] and scaled to 10 GHz, which is shown by the black dashed line in Fig. 4(a). Our low-loss *Process C* shows that sub-micron Nb interconnects can, remarkably, have R_s below R_{BCS} at 4.2 K, which can be attributed to the smearing of density of states.[74] Thus, *Processes B* and *C* demonstrate that a CMP planarized Nb interconnect can be scaled into submicron dimensions with no penalty above the minimum theoretical loss.

Figure 4(b) shows that all three processes yield approximately the same loss tangent tan$\delta \approx 1.2 \pm 0.1 \times 10^{-3}$ with virtually no MTL width dependence. This is in reasonable agreement with Kaiser,[37] who observed tan$\delta > 3 \times 10^{-4}$ for sputtered amorphous SiO_2 at 4.2 K, 1-10 GHz. Therefore, in spite of the same CVD parameters, TEOS-SiO_2 is not sensitive to significant differences between the three processes and offers a desirably large processing window.

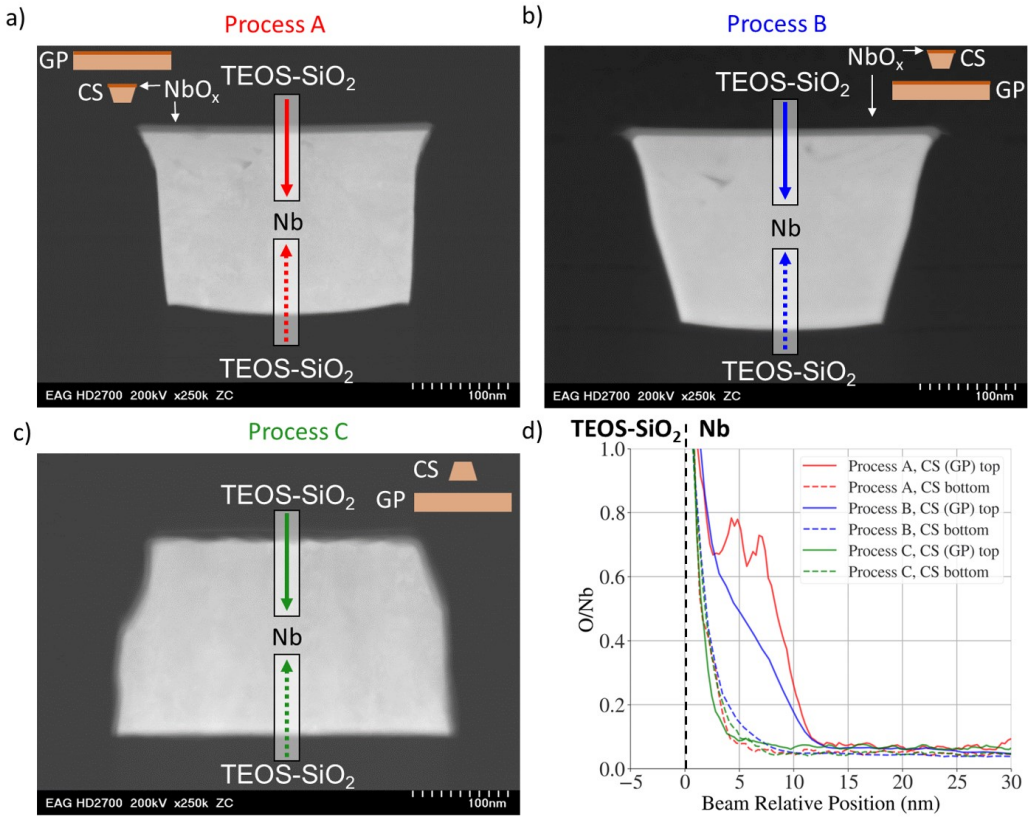

FIG. 5. STEM cross-sections of conducting strip for representative 0.25 μm MTL resonators fabricated by a) *Process A*, b) *Process B*, and c) *Process C*. The cartoons depict corresponding MTL geometry, showing NbO_x layers locations. d) EDS profiles of O/Nb content at the TEOS-SiO_2/Nb interface corresponding to line-cuts indicated by the colored arrows in a), b) and c). The zero of the beam relative position corresponds to the TEOS-SiO_2/Nb interface. We conjecture that the corresponding top *or* bottom surfaces of a conducting strip (CS) and a ground plane (GP) have the same O/Nb profile. All STEM and EDS characterizations were done at EAG Laboratories.[87]

A. R_{s0} variation with process

To explain the Nb loss variation with process seen in Fig. 4(a), we shall rely on a STEM complemented by an energy dispersive X-ray spectroscopy (EDS) with a 0.1-1 nm diameter electron beam and a detection limit of > 1 *at*%. Figure 5 shows STEM cross-sections of conducting strip looking into the 0.25 μm wide MTL, for all three processes. The analysis revealed that *Processes A* and *B* have 10-nm-thick Nb oxide (NbO_x) layer[88] on the top of both the ground plane and conducting strip, resulting from the oxygen plasma treatment to promote the TEOS-SiO_2 adhesion. FIB cross-sectioning showed that NbO_x has the same thickness in both the ground plane and conducting strip, for all five MTL widths. *Process C* has no visible NbO_x layers.

Figure 5 shows EDS line-cuts for the O/Nb content ratio at the top and bottom TEOS-SiO_2/Nb interfaces of a conducting strip, for all three processes. At the time of EDS data collection, it was deemed that only the conducting strip is of interest, so the EDS mapping for the ground plane was not requested. However, using same fabrication recipe for all metal layers in a chip, we suppose that the corresponding top *or* bottom surfaces of the conducting strip and ground plane have the same O/Nb profile, as conveyed in Fig. 5(d). Comparison of O/Nb profiles between the 0.25 μm and 1 μm conducting strips for *Processes A* and *C* suggests that for all three processes the profile is independent of MTL width.

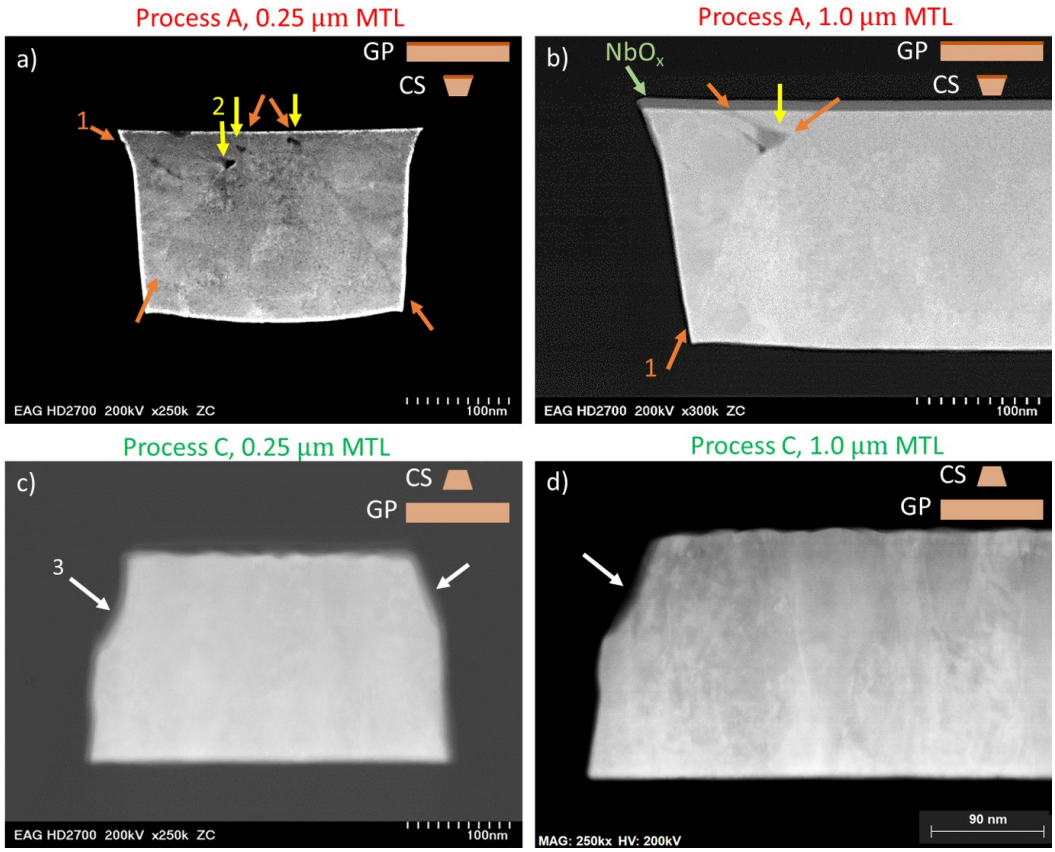

FIG. 6. STEM images taken for representative samples of a) 0.25 μm and b) 1 μm width MTL resonators from *Process A*, c) 0.25 μm and d) 1 μm width MTL resonators from *Process C*. For reference, the MTL geometry is shown on the top right of every image. Image contrast in a), b), and d) was enhanced to highlight features. Orange arrows in a) and b) indicate the intersection between two Nb growth directions due to a damascene process. Yellow arrows in a) and b) indicate voids and/or vacancies in Nb. White arrows in c) and d) indicate the "undercut" of the Nb during RIE. All STEM and EDS characterizations were done at EAG Laboratories.[87]

Figure 3(b) shows that for all MTL widths, the RF current concentrates in the ground plane and conducting strip near the TEOS-SiO_2/Nb interfaces facing each other. Hence, the MTL resistive loss is mostly sensitive to the oxygen content at such interfaces. For *Process A*, the oxygen content extends more than 10 nm into the top of the conducting strip, and diminishes within just few nanometers into the bottom of the ground plane. Conversely, for *Process B*, the oxygen content extends more than 10 nm into the ground plane top, and diminishes within just few nanometers into the conducting strip bottom. At the same time, the conducting strip top in *Process A* has a higher oxygen concentration than the ground plane top in *Process B*. Moreover, the inverted microstrip geometry of *Process A* makes NbO_x layer to overlap with the current density peaks at the edges of the conducting strip.[61]

These observations are consistent with about 2x difference in R_s between *Processes A* and *B* for all MTL widths.

For *Process C*, the oxygen content diminishes within just few nanometers into both the ground plane top and the conducting strip bottom. This is consistent with *Process C* exhibiting 30% lower R_s than *Process B* for all MTL widths but 4 μm. We also note that the rough surface of the conducting strip in *Process C* (see white arrows in Figs. 5(c) and 6(c),(d)) caused by the RIE undercut does not affect the R_s values.

B. R_{s0} up-turn at $0.25\,\mu m$ width

Another data trend seen in Fig. 4(a) is the 20-30% up-turn in R_s at 0.25 μm MTL width for *Processes A* and *B*. STEM cross-sections in Fig. 6(a),(b) show that the damascene process entails two Nb growth directions: vertical growth from the trench bottom and horizontal growth from the trench sidewall.[89] The two grain phases, a bottom grain and a sidewall grain, meet at about a 60° angle from the wafer plane. There are two such grain phase boundaries per conducting strip for both *Processes A* and *B*, indicated by orange arrows in Fig. 6(a),(b). Conversely, Fig. 6(c),(d) confirms that *Process C* exhibits only a vertically grown grain.

Aligned with the current flow in conducting strip, the grain phase boundaries may not affect the current distribution. At the same time, morphology of the sidewall grain may reduce the electron mean free path l_{mfp}, increasing the BCS resistance $R_{BCS} \propto (1+\xi_0/l_{mfp})^{\frac{3}{2}} l_{mfp}$, where $\xi_0 \sim 38\ nm$ is the microscopic coherence length in pure Nb. Moreover, Nb voids and vacancies at the grain phase boundaries, indicated by yellow arrows in Fig. 6(a),(b), may reduce l_{mfp} and increase R_{BCS}. The voids can also act as Nb hydride formation sites,[90] where hydrogen could diffuse into the Nb during fabrication, creating normal-conducting precipitates inside the conducting strip. Subject to proximity effect, hydrides suppress superconductivity in surrounding Nb.

Since the sidewall grain geometry is determined by the trench depth, decreasing MTL width increases both the sidewall grain and void fractions in the conducting strip cross-sectional area. For instance, the sidewall grain fraction increases from about 20% in a 1-μm-wide strip to about 50% in a 0.25-μm-wide strip. According to Fig. 3(c) and Eq. 13, the conducting strip contribution into the net R_s shown in Fig. 4(a) is the largest for a 0.25 μm MTL. Therefore, the R_s up-turn for 0.25 μm MTL in *Processes A* and *B* can be attributed to the sidewall grain phase and/or voids present in conducting strip.

VI. CONCLUSIONS

To conclude, we have developed a method to disentangle and quantify comparable superconductor and dielectric microwave losses by exploiting their frequency dependence in a multi-mode microstrip transmission line resonator representative of superconducting logic interconnects. The method was used to optimize a $0.25\,\mu m$ planarized process for minimum interconnect loss. With the aid of the geometric factor concept and the 3D superconductor HFSS modeling, the intrinsic resistance R_s was directly compared between different linewidths, stack geometries, and processing conditions. Correlating the Nb resistive loss with the STEM and EDS cross-sectional analysis revealed the mechanisms of loss above the microscopic theoretical minimum, including Nb oxide layer and Nb grain growth orientation.

We demonstrated that Nb interconnects can be scaled down to 0.25 μm linewidth with no penalty in microwave loss above the BCS minimum at 4.2 K. Nb sub-micron wires made by planarized Cloisonné process exhibit resistive loss $R_s = 13 \pm 1.4\ \mu\Omega$ at 4.2 K and 10 GHz, which is even lower than $R_s = 16 - 17\ \mu\Omega$ previously reported.[28,30,86] We found that dielectric loss tangent $\tan\delta = 1.2 \pm 0.1 \times 10^{-3}$ for TEOS-derived SiO_2 remains unaffected by MTL geometries and processing conditions. This makes it a very attractive interconnect insulator for highly-integrated superconductor circuits, although the dielectric loss is fairly high.

With Nb wires already at or below the theoretical minimum loss, it is worth exploring lower loss dielectrics compatible with the Nb fabrication. The energy efficiency of a ZOR metamaterial clock network relative to the RQL logic at 4.2 K and 10 GHz can be improved from 30%[11] up to 80-90% for Nb with $R_s = 13\ \mu\Omega$ and a dielectric with $\tan\delta \sim 10^{-4}$. Our loss data de-convolution method can be applied to any transmission line resonator including coplanar waveguide and stripline. We hypothesise that by increasing the resonator frequency range and number of modes, while improving the test probe bandwidth, one may unambiguously determine both the superconductor and dielectric loss frequency scaling

powers in Eq. 7, by allowing α and p as the fitting parameters.

ACKNOWLEDGEMENTS

The authors acknowledge Pavel Borodulin and Edward Kurek for assisting with test fixture design, Andrew Brownfield and David Vermillion for coordinating the test, Justin Goodman and Dr. Steve Sendelbach for assisting with data analysis, Dr. Eric Jones for the assistance with STEM and EDS analysis, Dr. Henry Luo for the penetration depth measurements by SQUID, and Dr. Flavio Griggio for the fruitful discussions. V.V.T. acknowledges insightful discussions with David Gill. S.M.A. acknowledges support from the National Science Foundation through Grant #NSF DMR-2004386, and the U.S. Department of Energy/High Energy Physics through grant #DESC0017931. This research is based on the work supported in part by the ODNI, IARPA, via ARO, contract #W911NF-14-C-0116. The views and conclusions contained herein are those of the authors and should not be interpreted as necessarily representing the official policies or endorsements, either expressed or implied, of the NSF, DOE, ODNI, IARPA, or the US Government. C.A.T.G. acknowledges approval for Public Release NG23-0122. © 2023 Northrop Grumman Systems Corporation

Appendix A: Derivation of Eq. 4

Ignoring the radiation loss, the internal Q-factor of a transmission line resonator can be expressed as[23]

$$\frac{1}{Q_i} = \frac{R}{\omega L} + \frac{G}{\omega C} \tag{A1}$$

where R and L are the line series resistance and inductance per unit length, G and C are the line shunt conductance and capacitance per unit length, and $\omega = 2\pi f$ is the angular frequency with f being the linear frequency. The telegrapher's equations have for the R, L, G, and C of a superconducting transmission line[23,61,91]

$$R = \frac{2}{|I|^2}\int_S R_s \lambda |\mathbf{J}|^2 \mathrm{d}s \approx \frac{2R_{eff}}{w} \tag{A2a}$$

$$L = \frac{\mu_0}{|I|^2}\int_S (|\mathbf{H}|^2 + \lambda^2 |\mathbf{J}|^2)\mathrm{d}s \approx \mu_0 \frac{s + 2\lambda_{eff}}{w} \tag{A2b}$$

$$G = \frac{\omega \varepsilon_0}{|V|^2}\int_S \tan\delta\, \varepsilon_r |\mathbf{E}|^2 \mathrm{d}s \approx \omega \varepsilon_0 \varepsilon_r \frac{w}{s} \tan\delta \tag{A2c}$$

$$C = \frac{\varepsilon_0}{|V|^2}\int_S \varepsilon_r |\mathbf{E}|^2 \mathrm{d}s \approx \varepsilon_0 \varepsilon_r \frac{w}{s} \tag{A2d}$$

where the integrals are carried over the line cross-section S, I and V are the line current and voltage, $\mathbf{J}$, $\mathbf{H}$ and $\mathbf{E}$ are the vector current density, magnetic field and electric field, R_s and λ are the intrinsic resistance and magnetic penetration depth, ε_0 and μ_0 are the vacuum permittivity and permeability, ε_r and $\tan\delta$ are the relative dielectric constant and the loss tangent, and it is assumed that $\sigma_1 \ll \sigma_2$ in Eqs. A2a and A2b. To provide a simple analytical reference, the approximations on the right of Eqs. A2 hold for a parallel-plate waveguide[30,33] formed by a dielectric spacer of thickness s sandwiched between two superconducting plates of thickness d and width $w \gg s$, with $R_{eff} = R_s[\coth(d/\lambda) + (d/\lambda)\,\mathrm{csch}^2(d/\lambda)]$ and $\lambda_{eff} = \lambda \coth(d/\lambda)$ being the plate effective surface resistance and effective penetration depth,[59] respectively.

Consider a uniform transmission line formed by M conductors, and N dielectric layers or tubes. Inserting Eqs. A2 into Eq. A1 yields

$$\frac{1}{Q_i} = \sum_{m=1}^{M} \frac{\overline{R_{sm}}}{\Gamma_{cm}} + \sum_{n=1}^{N} \frac{\overline{\tan\delta_n}}{\Gamma_{dn}} \tag{A3}$$

Here $\overline{R_{sm}}$ and $\overline{\tan\delta_n}$ are the averaged quantities describing loss in the m-th conductor and n-th dielectric,

$$\overline{R_{sm}} = \frac{\int_{S_{cm}} R_s \lambda |\mathbf{J}|^2 \mathrm{d}s}{\int_{S_{cm}} \lambda |\mathbf{J}|^2 \mathrm{d}s} \tag{A4a}$$

$$\overline{\tan\delta_n} = \frac{\int_{S_{dn}} \tan\delta\, \varepsilon_r |\mathbf{E}|^2 \mathrm{d}s}{\int_{S_{dn}} \varepsilon_r |\mathbf{E}|^2 \mathrm{d}s} \tag{A4b}$$

where S_{cm} and S_{dn} are the cross-sectional areas of the m-th conductor and n-th dielectric. In the case of the homogeneous losses (with arbitrary λ and ε_r distributions), $\overline{R_{sm}} = R_{sm}$ and $\overline{\tan\delta_n} = \tan\delta_n$. Furthermore, in Eq. A3, the partial geometric factors Γ_{cm} and Γ_{dn} associated with respective losses in the m-th conductor and n-th dielectric are

$$\Gamma_{cm} = \omega\mu_0 \frac{\int_S (|\mathbf{H}|^2 + \lambda^2 |\mathbf{J}|^2) \mathrm{d}s}{2\int_{S_{cm}} \lambda |\mathbf{J}|^2 \mathrm{d}s} \tag{A5a}$$

$$\Gamma_{dn} = \frac{\int_S \varepsilon_r |\mathbf{E}|^2 \mathrm{d}s}{\int_{S_{dn}} \varepsilon_r |\mathbf{E}|^2 \mathrm{d}s} \tag{A5b}$$

The conductor geometric factor Γ_c of a superconducting transmission line resonator has units of Ohm, and is defined exclusively by the line cross-sectional geometry and penetration depth λ. A good superconductor with $\sigma_1 \ll \sigma_2$ makes λ frequency independent, and so the fraction on the right of Eq. A5a. Note that definition A5a involves the field and current density inside the superconducting members. This differs from a cavity geometric factor[26,29,36]

$$\Gamma_{cav} = \omega\mu_0 \frac{\int_V |\mathbf{H}|^2 \mathrm{d}v}{\int_A |\mathbf{H}_\tau|^2 \mathrm{d}a} = \omega\mu_0 D \tag{A6}$$

which is governed by the ratio of the cavity volume V to the walls area A and involves magnetic field within that volume only, giving for the cavity Q-factor $Q = \Gamma_{cav}/R_s$. Equation A6 is applicable in the case of $D \gg \lambda$, where D is on the order of the cavity smallest dimension.[92] The concept of a cavity geometric factor is associated with Leontovich's impedance boundary condition $\mathbf{E}_\tau = Z_s \mathbf{H}_\tau \times \mathbf{n}$, where $\mathbf{E}_\tau$ and $\mathbf{H}_\tau$ are the respective tangential electric and magnetic fields at the impedance surface, and $\mathbf{n}$ is the inward unit vector normal to the surface.[55–58] The quantity Γ_c^{-1} can be seen as a transmission line counterpart of a conductor participation ratio Γ_{cav}^{-1} found in voluminous, cavity-like resonators.[39]

The dielectric geometric factor of a transmission line resonator given by Eq. A5b is unitless, and is defined exclusively by the line cross-sectional geometry and ε_r. The quantity Γ_d^{-1} can be seen as a transmission line counterpart of a dielectric filling factor found in the voluminous resonators[36,39]

$$p_{dn} = \frac{\int_{V_n} \varepsilon_r |\mathbf{E}|^2 \mathrm{d}v}{\int_V \varepsilon_r |\mathbf{E}|^2 \mathrm{d}v}$$

where V_n is the volume of the n-th dielectric ($n \geq 1$), and V is the volume of the entire resonator.

An embedded MTL like in Fig. 1(b) calls for $M = 2$ and $N = 2$ or 3 in Eq. A3, depending on the process. Assuming homogeneous losses within each of the conductor or dielectric

members, Eq. A3 gives rise to

$$\frac{1}{Q_i^A} = \frac{R_s^{gp}}{\Gamma_c^{gp}} + \frac{R_s^{cs}}{\Gamma_c^{cs}} + \frac{\tan\delta^{SiO2}}{\Gamma_d^{SiO2}} + \frac{\tan\delta^{Si}}{\Gamma_d^{Si}} \tag{A8a}$$

$$\frac{1}{Q_i^{B,C}} = \frac{R_s^{gp}}{\Gamma_c^{gp}} + \frac{R_s^{cs}}{\Gamma_c^{cs}} + \frac{\tan\delta^{SiO2}}{\Gamma_d^{SiO2}} + \frac{\tan\delta^{SiN}}{\Gamma_d^{SiN}} + \frac{\tan\delta^{LHe}}{\Gamma_d^{LHe}} \tag{A8b}$$

where Eqs. A8a and A8b correspond to *Process A* and *Processes B, C*, respectively. Furthermore, R_s^{gp} and R_s^{cs} are the intrinsic resistances of the ground plane and conducting strip, Γ_c^{gp} and Γ_c^{cs} are the partial geometric factors associated with resistive loss in respective conductors, $\tan\delta^{SiO2}$, $\tan\delta^{Si}$, $\tan\delta^{SiN}$ and $\tan\delta^{LHe}$ are the dielectric loss tangents of the TEOS-SiO_2 insulator, Si substrate, SiN_x passivation layer and LHe, respectively, and Γ_d^{SiO2}, Γ_d^{Si}, Γ_d^{SiN} and Γ_d^{LHe} are the partial geometric factors associated with loss in respective materials. Due to $\tan\delta^{SiN} \ll \tan\delta^{SiO2}, \tan\delta^{Si}, \tan\delta^{LHe}$[37], and $\Gamma_d^{SiO2} \ll \Gamma_d^{SiN}, \Gamma_d^{Si}, \Gamma_d^{LHe}$, the Si, SiN_x and LHe loss contributions can be ignored in Eqs. A8, both leading to Eq. 4.

Appendix B: Derivation of Eqs. 11

Consider a two-port network formed by a transmission line of length l. The ABCD (transmission) matrix of such network is[93]

$$\begin{bmatrix} A & B \\ C & D \end{bmatrix} = \begin{bmatrix} \cosh(\gamma l) & Z_{TL}\sinh(\gamma l) \\ Z_{TL}^{-1}\sinh(\gamma l) & \cosh(\gamma l) \end{bmatrix} \tag{B1}$$

where γ is the propagation constant, and Z_{TL} is the characteristic impedance. For the electrically short network, a quadratic Taylor expansion around $\gamma l = 0$ yields $\cosh(\gamma l) \approx 1 + (\gamma l)^2/2$ and $\sinh(\gamma l) \approx \gamma l$. A general transmission line has[85] $\gamma = \sqrt{ZY}$ and $Z_{TL} = \sqrt{Z/Y}$, where Z and Y are the series impedance and shunt admittance per unit length. Inserting all of the above into Eq. B1 gives

$$\begin{bmatrix} A & B \\ C & D \end{bmatrix} \approx \begin{bmatrix} 1 + ZYl^2/2 & Zl \\ Yl & 1 + ZYl^2/2 \end{bmatrix} \tag{B2}$$

By reciprocity, the elements of the [Z]-matrix corresponding to the ABCD matrix[23] given by Eq. B2 are $Z_{11} = Z_{22} = (Yl)^{-1} + Zl/2$ and $Z_{12} = Z_{21} = (Yl)^{-1}$. Solving these for the Z and Y yields Eqs. 11.

[1]K. Likharev, O. Mukhanov, and V. Semenov, "Resistive single flux quantum logic for the josephson-junction digital technology," SQUID Journal **85**, 1103–1108 (1985).
[2]K. K. Likharev and V. K. Semenov, "Rsfq logic/memory family: A new josephson-junction technology for sub-terahertz-clock-frequency digital systems," IEEE Transactions on Applied Superconductivity **1**, 3–28 (1991).
[3]M. Hosoya, W. Hioe, J. Casas, R. Kamikawai, Y. Harada, Y. Wada, H. Nakane, R. Suda, and E. Goto, "Quantum flux parametron: a single quantum flux device for josephson supercomputer," IEEE Transactions on Applied Superconductivity **1**, 77–89 (1991).
[4]Q. P. Herr, A. Y. Herr, O. T. Oberg, and A. G. Ioannidis, "Ultra-low-power superconductor logic," Journal of applied physics **109**, 103903 (2011).
[5]M. H. Volkmann, A. Sahu, C. J. Fourie, and O. A. Mukhanov, "Implementation of energy efficient single flux quantum digital circuits with sub-aj/bit operation," Superconductor Science and Technology **26**, 015002 (2012).
[6]N. Takeuchi, D. Ozawa, Y. Yamanashi, and N. Yoshikawa, "An adiabatic quantum flux parametron as an ultra-low-power logic device," Superconductor Science and Technology **26**, 035010 (2013).
[7]R. Peterson and D. McDonald, "Picosecond pulses from josephson junctions: Phenomenological and microscopic analyses," IEEE Transactions on Magnetics **13**, 887–890 (1977).
[8]Y. Yamanashi, T. Kainuma, N. Yoshikawa, I. Kataeva, H. Akaike, A. Fijumaki, M. Tnaka, N. Takagi, S. Nagasawa, and M. Hidaka, "100 GHz demonstrations based on the single-flux-quantum cell library for the 10 kA/cm2 nb multi-layer process," IEICE Transactions on Electronics **E93-C**, 440–444 (2010).
[9]S. K. Tolpygo, "Superconductor digital electronics: Scalability and energy efficiency issues (review article)," Low Temperature Physics **42**, 361–379 (2016).
[10]L. Chang, D. J. Frank, R. K. Montoye, S. J. Koester, B. L. Ji, P. W. Coteus, R. H. Dennard, and W. Haensch, "Practical strategies for power-efficient computing technologies," Proceedings of the IEEE **98**, 215–236 (2010).
[11]J. A. Strong, V. V. Talanov, M. E. Nielsen, A. C. Brownfield, N. Bailey, Q. P. Herr, and A. Y. Herr, "A resonant metamaterial clock distribution network for superconducting logic," Nature Electronics **5**, 171–177 (2022).
[12]I. R. F. DEVICES and SYSTEMS, "Cryogenic electronics and quantum information processing," (2020).
[13]A. Ramzi, S. A. Charlebois, and P. Krantz, "Niobium and aluminum josephson junctions fabricated with a damascene cmp process," Physics Procedia **36**, 211–216 (2012).
[14]S. Nagasawa, T. Satoh, K. Hinode, Y. Kitagawa, M. Hidaka, H. Akaike, A. Fujimaki, K. Takagi, N. Takagi, and N. Yoshikawa, "New nb multi-layer fabrication process for large-scale sfq circuits," Physica C: Superconductivity **469**, 1578–1584 (2009).
[15]C. Kaanta, W. Cote, J. Cronin, K. Holland, P.-I. Lee, and T. Wright, "Submicron wiring technology with tungsten and planarization," in *1987 International Electron Devices Meeting* (IEEE, 1987) pp. 209–212.
[16]W. L. Guthrie, W. J. Patrick, E. Levine, H. C. Jones, E. A. Mehter, T. F. Houghton, G. T. Chiu, and M. A. Fury, "A four-level vlsi bipolar metallization design with chemical-mechanical planarization," IBM journal of research and development **36**, 845–857 (1992).
[17]M. Krishnan, J. W. Nalaskowski, and L. M. Cook, "Chemical mechanical planarization: slurry chemistry, materials, and mechanisms," Chemical reviews **110**, 178–204 (2010).
[18]J. Egan, M. Nielsen, J. Strong, V. V. Talanov, E. Rudman, B. Song, Q. Herr, and A. Herr, "Synchronous chip-to-chip communication with a multi-chip resonator clock distribution network," arXiv preprint arXiv:2109.00560 (2021).
[19]H. Dai, C. Kegerreis, D. W. Gamage, J. Egan, M. Nielsen, Y. Chen, D. Tuckerman, S. Peek, B. Yelamanchili, M. Hamilton, *et al.*, "Isochronous data link across a superconducting nb flex cable with 5 femtojoules per bit," Superconductor Science and Technology (2022).
[20]R. L. Kautz, "Picosecond pulses on superconducting striplines," Journal of Applied Physics **49**, 308–314 (1978).
[21]V. V. Talanov, D. Knee, D. Harms, K. Perkins, A. Urbanas, J. Egan, Q. Herr, and A. Herr, "Propagation of picosecond pulses on superconducting transmission line interconnects," Superconductor Science and Technology **35**, 055011 (2022).
[22]G. Tzimpragos, J. Volk, A. Wynn, E. Golden, and T. Sherwood, "Pulsar: A superconducting delay-line memory," arXiv preprint arXiv:2205.08016 (2022).
[23]D. M. Pozar, *Microwave engineering*, 4th ed. (John wiley & sons, 2011).
[24]W. M. Fairbank, "High frequency surface resistivity of tin in the normal and superconducting states," Physical Review **76**, 1106 (1949).
[25]E. Maxwell, P. Marcus, and J. C. Slater, "Surface impedance of normal and superconductors at 24,000 megacycles per second," Physical Review **76**, 1332 (1949).
[26]J. Turneaure, J. Halbritter, and H. Schwettman, "The surface impedance of superconductors and normal conductors: The mattis-bardeen theory," Journal of Superconductivity **4**, 341–355 (1991).
[27]N. Newman and W. G. Lyons, "High-temperature superconducting microwave devices: fundamental issues in materials, physics, and engineering," Journal of Superconductivity **6**, 119–160 (1993).
[28]C. Benvenuti, S. Calatroni, I. Campisi, P. Darriulat, M. Peck, R. Russo, and A.-M. Valente, "Study of the surface resistance of superconducting niobium films at 1.5 ghz," Physica C: Superconductivity **316**, 153–188 (1999).

[29]M. Hein, *High-temperature-superconductor thin films at microwave frequencies*, Vol. 155 (Springer Science & Business Media, 1999).
[30]R. Taber, "A parallel plate resonator technique for microwave loss measurements on superconductors," Review of scientific instruments **61**, 2200–2206 (1990).
[31]J. S. Martens, V. M. Hietala, D. S. Ginley, T. E. Zipperian, and G. K. G. Hohenwarter, "Confocal resonators for measuring the surface resistance of high-temperature superconducting films," Applied Physics Letters **58**, 2543–2545 (1991).
[32]J. Mazierska, "Dielectric resonator as a possible standard for characterization of high temperature superconducting films for microwave applications," Journal of Superconductivity **10**, 73–84 (1997).
[33]V. V. Talanov, L. V. Mercaldo, S. M. Anlage, and J. H. Claassen, "Measurement of the absolute penetration depth and surface resistance of superconductors and normal metals with the variable spacing parallel plate resonator," Review of Scientific Instruments **71**, 2136–2146 (2000).
[34]S. M. Anlage, "Microwave superconductivity," IEEE Journal of Microwaves **1**, 389–402 (2021).
[35]C. Zuccaro, M. Winter, N. Klein, and K. Urban, "Microwave absorption in single crystals of lanthanum aluminate," Journal of Applied Physics **82**, 5695–5704 (1997).
[36]J. Krupka, K. Derzakowski, B. Riddle, and J. Baker-Jarvis, "A dielectric resonator for measurements of complex permittivity of low loss dielectric materials as a function of temperature," Measurement Science and Technology **9**, 1751 (1998).
[37]C. Kaiser, *High quality Nb/Al-AlOx/Nb Josephson junctions: technological development and macroscopic quantum experiments*, Vol. 4 (KIT Scientific Publishing, 2011).
[38]D. B. Tuckerman, M. C. Hamilton, D. J. Reilly, R. Bai, G. A. Hernandez, J. M. Hornibrook, J. A. Sellers, and C. D. Ellis, "Flexible superconducting nb transmission lines on thin film polyimide for quantum computing applications," Superconductor Science and Technology **29**, 084007 (2016).
[39]C. R. H. McRae, H. Wang, J. Gao, M. R. Vissers, T. Brecht, A. Dunsworth, D. P. Pappas, and J. Mutus, "Materials loss measurements using superconducting microwave resonators," Review of Scientific Instruments **91**, 091101 (2020).
[40]D. R. Young, J. C. Swihart, S. Tansal, and N. H. Meyers, "Use of a superconducting transmission line for measuring penetration depths," Solid-State Electronics **1**, 378–380 (1960).
[41]P. V. Mason and R. W. Gould, "Slow-wave structures utilizing superconducting thin-film transmission lines," Journal of Applied Physics **40**, 2039–2051 (1969).
[42]W. Henkels and C. Kircher, "Penetration depth measurements on type ii superconducting films," Magnetics, IEEE Transactions on **13**, 63–66 (1977).
[43]S. M. Anlage, H. Sze, H. J. Snortland, S. Tahara, B. Langley, C.-B. Eom, M. Beasley, and R. Taber, "Measurements of the magnetic penetration depth in yba2cu3o7- δ thin films by the microstrip resonator technique," Applied physics letters **54**, 2710–2712 (1989).
[44]B. W. Langley, S. M. Anlage, R. F. W. Pease, and M. R. Beasley, "Magnetic penetration depth measurements of superconducting thin-films by a microstrip resonator technique," Review of Scientific Instruments **62**, 1801–1812 (1991).
[45]A. Megrant, C. Neill, R. Barends, B. Chiaro, Y. Chen, L. Feigl, J. Kelly, E. Lucero, M. Mariantoni, P. J. O'Malley, *et al.*, "Planar superconducting resonators with internal quality factors above one million," Applied Physics Letters **100**, 113510 (2012).
[46]M. S. Khalil, M. Stoutimore, F. Wellstood, and K. Osborn, "An analysis method for asymmetric resonator transmission applied to superconducting devices," Journal of Applied Physics **111**, 054510 (2012).
[47]E. Belohoubek and E. Denlinger, "Loss considerations for microstrip resonators (short papers)," IEEE Transactions on Microwave Theory and Techniques **23**, 522–526 (1975).
[48]D. E. Oates, S. K. Tolpygo, and V. Bolkhovsky, "Submicron nb microwave transmission lines and components for single-flux-quantum and analog large-scale superconducting integrated circuits," IEEE Transactions on Applied Superconductivity **27**, 1–5 (2017).
[49]J. Krupka, J. Breeze, A. Centeno, N. Alford, T. Claussen, and L. Jensen, "Measurements of permittivity, dielectric loss tangent, and resistivity of float-zone silicon at microwave frequencies," IEEE Transactions on microwave theory and techniques **54**, 3995–4001 (2006).
[50]G. Yassin and S. Withington, "Electromagnetic models for superconducting millimetre-wave and sub-millimetre-wave microstrip transmission lines," Journal of Physics D: Applied Physics **28**, 1983–1991 (1995).
[51]M. R. Rafique, I. Kataeva, H. Engseth, M. Tarasov, and A. Kidiyarova-Shevchenko, "Optimization of superconducting microstrip interconnects for rapid single-flux-quantum circuits," Superconductor Science and Technology **18**, 1065–1072 (2005).
[52]V. Belitsky, C. Risacher, M. Pantaleev, and V. Vassilev, "Superconducting microstrip line model studies at millimetre and sub-millimetre waves," International journal of infrared and millimeter waves **27**, 809–834 (2006).
[53]K. U-Yen, K. Rostem, and E. J. Wollack, "Modeling strategies for superconducting microstrip transmission line structures," IEEE Transactions on Applied Superconductivity **28**, 1–5 (2018).
[54]M. H. Amini and A. Mallahzadeh, "Modeling of superconducting components in full-wave simulators," Journal of Superconductivity and Novel Magnetism **34**, 675–681 (2021).
[55]M. Leontovich, "A new method to solve problems of em wave propagation over the earth surface," USSR Academy of Sciences Trans., Physics Series **8**, 16–22 (1944).

[56]M. Leontovich, "Approximate boundary conditions for the electromagnetic field on the surface of a good conductor," Investigations on Radiowave Propagation **2**, 5–12 (1948).
[57]T. Senior, "Impedance boundary conditions for imperfectly conducting surfaces," Applied Scientific Research, Section B **8**, 418–436 (1960).
[58]M. A. Miller and V. I. Talanov, "The use of the surface impedance concept in the theory of electromagnetic surface waves," (in Russian) Izvestia VUZov Radiofizika **4**, 795–830 (1961), [Onde superficiali, Springer Berlin Heidelberg, 2011, pp. 257–347].
[59]N. Klein, H. Chaloupka, G. Müller, S. Orbach, H. Piel, B. Roas, L. Schultz, U. Klein, and M. Peiniger, "The effective microwave surface impedance of high t c thin films," Journal of Applied Physics **67**, 6940–6945 (1990).
[60]D. C. Mattis and J. Bardeen, "Theory of the anomalous skin effect in normal and superconducting metals," Physical Review **111**, 412 (1958).
[61]D. M. Sheen, S. M. Ali, D. E. Oates, R. S. Withers, and J. Kong, "Current distribution, resistance, and inductance for superconducting strip transmission lines," IEEE Transactions on Applied Superconductivity **1**, 108–115 (1991).
[62]Release 2021 R2, *HFSS*, ANSYS, Canonsburg, PA (2021).
[63]J. C. Swihart, "Field solution for a thin-film superconducting strip transmission line," Journal of Applied Physics **32**, 461–469 (1961).
[64]S. M. Anlage and D. H. Wu, "Magnetic penetration depth measurements in cuprate superconductors," Journal of Superconductivity **5**, 395–402 (1992).
[65]O. Rocha, C. Viana, L. Gonçalves, and N. Morimoto, "Electrical characteristics of pecvd silicon oxide deposited with low teos contents at low temperatures," 2004 Microelectronics Technology and Devices SBMICRO , 295–300 (2004).
[66]H. Luo, *Modelling and Measurement of Reciprocal Quantum Logic Circuits*, Ph.D. thesis, University of Maryland College Park (2021).
[67]S. K. Tolpygo, E. B. Golden, T. J. Weir, and V. Bolkhovsky, "Inductance of superconductor integrated circuit features with sizes down to 120 nm," Superconductor Science and Technology **34**, 085005 (2021).
[68]A. Khanna and Y. Garault, "Determination of loaded, unloaded, and external quality factors of a dielectric resonator coupled to a microstrip line," IEEE Transactions on Microwave Theory and Techniques **31**, 261–264 (1983).
[69]D. R. Cote, S. Nguyen, W. J. Cote, S. L. Pennington, A. K. Stamper, and D. V. Podlesnik, "Low-temperature chemical vapor deposition processes and dielectrics for microelectronic circuit manufacturing at ibm," IBM Journal of Research and Development **39**, 437–464 (1995).
[70]C. C. Chin, D. E. Oates, G. Dresselhaus, and M. S. Dresselhaus, "Nonlinear electrodynamics of superconducting nbn and nb thin films at microwave frequencies," Phys. Rev. B **45**, 4788–4798 (1992).
[71]M. A. Golosovsky, H. J. Snortland, and M. R. Beasley, "Nonlinear microwave properties of superconducting nb microstrip resonators," Phys. Rev. B **51**, 6462–6469 (1995).
[72]W. Jutzi, S. Wuensch, E. Crocoll, M. Neuhaus, T. Scherer, T. Weimann, and J. Niemeyer, "Microwave and dc properties of niobium coplanar waveguides with 50-nm linewidth on silicon substrates," IEEE transactions on applied superconductivity **13**, 320–323 (2003).
[73]P. J. Petersan and S. M. Anlage, "Measurement of resonant frequency and quality factor of microwave resonators: Comparison of methods," Journal of Applied Physics **84**, 3392–3402 (1998).
[74]A. Philipp and J. Halbritter, "Investigation of the gap edge density of states at oxidized niobium surfaces by rf measurements," IEEE Transactions on Magnetics **19**, 999–1002 (1983).
[75]A. K. Jonscher, "The 'universal' dielectric response," nature **267**, 673–679 (1977).
[76]J. Baker-Jarvis, M. D. Janezic, B. Riddle, and S. Kim, "Behavior of $\acute{\varepsilon}$ (ω) and tan δ for a class of low-loss materials," in *CPEM 2010* (IEEE, 2010) pp. 289–290.
[77]W. Chang, "The inductance of a superconducting strip transmission line," Journal of Applied Physics **50**, 8129–8134 (1979).
[78]Y. Guo, D. Kim, J. He, S. Yong, Y. Liu, X. Ye, and J. Fan, "Limitations of first-order surface impedance boundary condition and its effect on 2d simulations for pcb transmission lines," in *2020 IEEE International Symposium on Electromagnetic Compatibility & Signal/Power Integrity (EMCSI)* (IEEE, 2020) pp. 422–427.
[79]K. K. Mei and G.-C. Liang, "Electromagnetics of superconductors," IEEE transactions on microwave theory and techniques **39**, 1545–1552 (1991).
[80]At the time of this work, the most recent version of HFSS that permits material with complex conductivity and removes a need for PEC ports, was unavailable.
[81]T. M. Mishonov, "Predicted plasma oscillations in the $bi_2sr_2cacu_2o_8$ high-temperature superconductor," Physical Review B **44**, 12033–12034 (1991).
[82]For niobium, ω_p is above the superconducting gap frequency.
[83]R. Glover III and M. Tinkham, "Conductivity of superconducting films for photon energies between 0.3 and 40 kt_c," Physical Review **108**, 243 (1957).
[84]C. A. T. Garcia, *Materials Characterization for Sub-micron Superconducting Interconnects in Reciprocal Quantum Logic Circuits*, Ph.D. thesis, University of Maryland, College Park (2022).
[85]S. Ramo, J. R. Whinnery, and T. Van Duzer, *Fields and waves in communication electronics* (John Wiley & Sons, 1994).
[86]L. R. Group, *SRIMP*, Cornell Univ. (2012).

[87]LABS, *EAG*, EAG (2022).
[88]J. Halbritter, "On the oxidation and on the superconductivity of niobium," Applied Physics A Solids and Surfaces **43**, 1–28 (1987).
[89]S.-P. Ju, C.-I. Weng, J.-G. Chang, and C.-C. Hwang, "Molecular dynamics simulation of sputter trench-filling morphology in damascene process," Journal of Vacuum Science & Technology B: Microelectronics and Nanometer Structures Processing, Measurement, and Phenomena **20**, 946–955 (2002).
[90]A. Romanenko, C. Edwardson, P. Coleman, and P. Simpson, "The effect of vacancies on the microwave surface resistance of niobium revealed by positron annihilation spectroscopy," Applied Physics Letters **102**, 232601 (2013).
[91]A. Sass and W. Stewart, "Self and mutual inductances of superconducting structures," Journal of Applied Physics **39**, 1956–1963 (1968).
[92]L. A. Vainshtein, *Electromagnetic waves*, 2nd ed. (Moscow, Izdatel'stvo Radio i Sviaz', In Russian, 1988).
[93]C. R. Paul, *Analysis of multiconductor transmission lines* (John Wiley & Sons, 2007).